Numerical and Experimental Analysis of the Cold Flow Physics of a Nonpremixed Industrial Gas Burner

A. Ortolani*
Ph.D. Student
Department of Engineering
University of Lancaster
Lancaster, United Kingdom LA1 4YW
Email: a.ortolani@lancaster.ac.uk

J. Yeadon
Proctor Process Plant Ltd.
Burnley, United Kingdom BB11 5UB

B. Ruane
Proctor Process Plant Ltd.
Burnley, United Kingdom BB11 5UB

M. Paul
Professor
School of Engineering
University of Glasgow
Glasgow, United Kingdom G12 8QQ
Email: manosh.Paul@glasgow.ac.uk

M.S. Campobasso
Associate professor
Department of Engineering
University of Lancaster
Lancaster, United Kingdom LA1 4YW
Email: m.s.campobasso@lancaster.ac.uk

*Corresponding author

ABSTRACT

The flow field of a non-premixed industrial gas burner is analyzed with Reynolds-averaged Navier Stokes computational fluid dynamics validated against velocity and pressure measurements. Combustion is not modeled because the aim is optimizing the predictive capabilities of the cold flow before including chemistry. The system's complex flow physics, affected by a 90° turn, backward and forward facing steps, and transversal jets in the main stream is investigated at full and partial load. The sensitivity of the computed flow field to inflow boundary condition set-up, approach for resolving/modeling wall bounded flows, and turbulence closure is assessed. In the first sensitivity analysis, the inflow boundary condition is prescribed using measured total pressure or measured velocity field. In the second, boundary layers are resolved down to the wall or modeled with wall functions. In the third sensitivity analysis, the turbulence closure uses the $k-\omega$ *shear stress transport eddy viscosity model or two variants of the Reynolds stress model. The agreement between the predictions of most simulation set-ups among themselves and with the measurements is good. For given type of inflow condition and wall flow treatment, the* ω*-based Reynolds stress model gives the best agreement with measurements among the considered turbulence models at full load. At partial load, the comparison with measured data highlights some scatter in the predictions of different patterns of the flow measurements. Overall, the findings of this study provide insight into the fluid dynamics of industrial gas burners, and guidelines for their simulation-based analysis.*

Keywords: Industrial gas burner fluid dynamics, Navier-Stokes Computational Fluid Dynamics, Reynolds-stress and $k-\omega$ SST turbulence models, Pressure and velocity measurements

1 Introduction

Turbulent combustion sits at the interface of the chemistry and turbulence disciplines, both characterized by a key role of nonlinearity and multi-scale phenomena. This makes the simulations of turbulent combustion processes based on Computational Fluid Dynamics (CFD) a challenging task, even when the chemical mechanisms at work are well known. For example, this is the case of methane-air diffusion flames, which have been the focus of intense research for several years. In this field, many simulation studies have focused on relatively simple laboratory experiments in well controlled conditions, such as the Sandia flames [1–3]. Despite the apparent simplicity of this reactive flow, the prediction of some of its features, including the formation of pollutants such as nitrogen oxides, remains a difficult task. These modeling challenges may be higher when using the Reynolds-Averaged Navier Stokes (RANS) approach [4,5], rather than the higher-fidelity Large Eddies Simulation (LES) approach [6, 7]. This is because a necessary prerequisite for reliable predictions of turbulent combustion is a sufficient resolution of flow turbulence, an aim achievable more easily by using LES, which resolves the larger scales of turbulence. Unfortunately, the computational burden of LES is higher than that of RANS simulations, and therefore LES is often not amenable to industrial applications. On the other hand, a wide fidelity spectrum also exists in the domain of RANS methods, and the RANS simulation outcome is also affected by several modeling choices. Thus, it is of interest to keep improving the RANS methodology for turbulent combustion analysis and burner design.

Most industrial burners are characterized by geometries and flow fields which are far more complex than those of reference laboratory experiments, such as the Sandia Flames. In industrial applications, it is important to optimize and validate the predictive capabilities of the CFD analysis of the cold flow of the system, ie that without chemistry, before including also reactive flow modeling in the simulations. This is because the levels and patterns of flow turbulence have a strong impact on the predictions of the combustion process [8]. Recently, this approach was adopted by Wronski et al. [9], who analyzed the cold flow field of a magnesium burner performing RANS analyses with the CFD code ANSYS FLUENT. To avoid handling simultaneously the uncertainty affecting the analysis of swirling flows in geometrically complex ducts, and that associated with modeling the combustion of the two-phase flow of magnesium and air, they started their investigations by modeling the cold one-phase swirling air flow. The authors compared the results of their simulations with experimental data that they obtained for two operating conditions, characterized by different levels of flow swirl. They tested several variants of the $k-\varepsilon$ turbulence model [10] and of the Reynolds Stress Model (RSM) [11]. It was found that, for the low-swirl case, the Renormalization Group $k-\varepsilon$ turbulence model [10] performed slightly better than the other variants. In the high swirl case, the RSM variant based on the ω-equation of the standard $k-\omega$ [12] gave the best predictions. In both cases, the shape and position of the zone with negative values of axial velocity in the main duct could be predicted with reasonable accuracy.

Meraner et al. [13] conducted a numerical study of the cold flow in a partially premixed bluff body burner, and compared their computed velocity fields with the Particle Image Velocimetry measurements of Dutka et al. [14]. The authors tested three RANS eddy viscosity turbulence models, namely the standard $k-\varepsilon$ model, the realizable $k-\varepsilon$ model [15] and the $k-\omega$ Shear Stress Transport (SST) [16]. An overall good agreement with experiments was found, particularly with regard to the size of the flow recirculation region behind the bluff body. However, the predicted magnitude of the axial velocity deviated from the experimental data. The $k-\omega$ SST model performed better than the other two models in capturing the velocity decay in the jet region downstream of the recirculation zone, but worst in terms of predicting the overall velocity level. The agreement between SST-based predictions and experiments improved when the analysis was carried out in unsteady mode. Even larger improvements were observed using LES and a stress-blended eddy simulation (SBES) [17, 18].

The general aim of this study, which is part of a wider ongoing research, is to develop an experimentally validated computationally affordable RANS CFD technology for the analysis and design of industrial gas burners. The objective of the analyses herein is two-fold: on one hand, it is to investigate and shed light on the complex fluid dynamics of an industrial gas burner, supporting the findings on its flow physics with measurements of its flow field; on the other hand, the objective is to present parametric analyses of the simulation set-up, including inflow boundary condition (BC) choice, approach to the solution of wall-bounded flows, and turbulence closure, and provide guidelines on the best choices in RANS CFD simulations of industrial gas burners. The investigation focuses on the nonreactive flow of the burner because of the importance of an adequate prediction of turbulent flow patterns to reliably predict turbulent combustion problems, as discussed above. The considered test case is a non-premixed industrial burner for natural gas and methane combustion. The burner is designed to operate in continuous industrial processes with a firing range from 12 to 120 KW. The flow simulations and measurements of this study refer to two load conditions using only air as working fluid. The main novelty of this study is the investigation of the cold flow physics of a non-premixed industrial gas burner, and its dependence on the operating condition. Since the control of the turbulent flow pattern is one of the means available to improve the efficiency and reduce the emissions of this system, predicting and explaining the key flow features is paramount to its design optimization. The experimental part of this investigation is carried out by using a full-scale test rig that reproduces the conditions in which the gas burner is operated in production. This makes the presented analyses relevant to both the scientific and industrial communities of this sector.

The outline of the paper is as follows. Section 2 presents the test rig and a general description of the fluid flow paths in this case study. In Section 3 the experimental set-up and the procedure followed for the measurements are described. Section 4 describes the CFD code and methodology, whereas Section 5 defines the physical domain, grids, and BCs. Section 6 assesses the grid independence of the CFD solutions. Section 7 presents the results of this study: first, the main findings of the parametric analyses varying inlet BC, calculation of the wall-bounded flows, and turbulence models are presented; then the main features of the flow field of the system are presented and discussed. Finally, Section 8 provides a summary of the study with comments on future work.

2 Test Rig

The outer geometry of the considered burner, consisting of a case containing part of the nozzle, is reported in Fig. 1a. A fan, connected to the burner with an inlet duct, provides the air flow supply (Fig. 1b). The fan works at constant angular speed, with the air flow rate being regulated by a throttling valve located just before the case. The inlet duct has a rectangular cross section equal to that of the throttling valve case. Figure 1b also shows the combustion chamber bolted to the burner case. The chamber has a cylindrical shape and it is open on the outlet section, communicating directly with the external ambient. Figure 2a shows that the nozzle consists of a conical part surrounded by a coaxial cylinder. The cone has several holes arranged in a periodic pattern. Figure 2a also highlights a flame detector, and a spark plug. Together with some bolts, these two components are the only elements breaking the axial symmetry of the nozzle geometry.

[FIGURE 1]

The schematic of Fig. 2b shows the flow path in the burner. The stream of fresh air enters the case, and after a 90° turn, it splits into multiple co-axial streams. The innermost stream flows in a tube (”nozzle inlet duct”) whose axis lays on the centerline of the chamber. This is the stream indicated by the central black arrow. This stream then passes through the nozzle and reaches the combustion chamber. Most of the remaining air enters the chamber through the holes on the conical part of the nozzle. Secondary air streams enter in the combustion chamber following two different paths: the small gap between the external face of the cylinder and the burner case, and the gap between the internal face of the cylinder and the cone. When the burner is firing, the fuel stream follows the path of the striped arrows in Fig. 2b, guided by the fuel system ducts shown in Fig. 2a. The fuel mixes with the air directly in the nozzle, and in this way, it feeds the flame.

[FIGURE 2]

Since this study focuses on the cold flow field of the considered system, the fuel inlet is disconnected from the fuel supply. It is also sealed so that no air enters from there. In this way, the fuel inlet box communicates only with the nozzle via the fuel duct shown in Fig. 2a.

Figure 3 provides the symbols used in this study to denote the characteristic lengths of the system. The diameter and the length of the cylindrical combustion chamber, not reported in Fig. 3, are denoted by d_c and l_c, respectively. Table 1 reports all characteristic lengths normalized with the nozzle external diameter d_n, which equals 125mm.

[FIGURE 3]

[TABLE 1]

3 Experimental set-up

The measured quantities in this study are static pressure, total pressure, and velocity. Flush-mounted pressure taps are used to measure the static pressure. The probe used to measure the total pressure consists of a tube with a hole whose axis is oriented as the incoming flow. Both static and total pressures are measured with the SDP816-500PA analog transducer by Sensirion [19]. This sensor measures the difference between probed and ambient pressures, and it outputs an analog ratiometric voltage. The sensor covers a range of $\pm 500Pa$ with an accuracy of $\pm 3\%$ of the measured value $\pm 0.1Pa$. Five of these transducers are connected to an Arduino board and collect 500 samples of static or total pressures with a sampling frequency of $5.4Hz$. In this study, the static and total pressures measured with these transducers are labeled ”SDP816”.

Some static and total pressure measurements are repeated with a second differential manometer to verify the calibration of the SDP816 transducer. For this purpose, the Kimo MP 200 P manometer [20], characterized by a range of $\pm 500Pa$ with an accuracy equal to $\pm 0.2\%$ of the measured value $\pm 1.5Pa$, is used. This manometer measures the difference between probed and ambient pressures, and outputs its value on a screen. As this sensor does not have data-logging capability, an average pressure value is computed with 10 screen readings. In this study, the static and total pressures measured with this manometer are labeled ”Kimo”. Unless otherwise stated, the measured pressure data reported below are the SDP816 transducer.

A constant-temperature thermal anemometer, namely the TA440 model by TSI Incorporated [21], measures the velocity along the desired direction. The measured velocity component depends on the orientation of the probe. The measuring range of this sensor goes from 0 to $30\frac{m}{s}$ with an accuracy of $\pm 3\%$ of the measured value and a resolution of $0.01\frac{m}{s}$. The anemometer has a sampling frequency of $1Hz$. This sensor measures time-averaged values of the velocity over $1s$. Each measurement is carried out for more than $5min$, providing velocity time-histories consisting of over 300 samples.

All measured time-series are elaborated to compute the mean value and the Root-Mean-Square (RMS) of the deviations from such mean value at each measurement point. The measured quantities presented in the following Sections 5 and 7, unless otherwise stated, are in form of time-averaged values.

The measurement locations are divided into three subsets or *stations* to help the discussion. Each station consists of all the measurements carried out in one region of the test rig. Station 1 is located at the mid length of the inlet duct, and is depicted in Fig. 4. Here the sensors are used to measure velocity and total pressure with the aim of providing data for the inlet BCs of the CFD simulations. Both quantities are measured at five positions, indicated by black dots in Fig. 4. The orientation of the probes is such that they capture the component of the flow velocity in the Y direction. The X and Z velocity components are neglected. The static pressure is measured on the midpoint of each side of the measuring section (white dots in Figure 4).

[FIGURE 4]

Figure 5 provides a schematic of the station 2, showing the locations at which the static pressure is measured on the burner case. A pressure tap is positioned on the fuel box (FB), as its pressure provides an indirect measure of the velocity in the nozzle itself. This method allows collecting information on the flow in the nozzle in a non-intrusive way. The figure also shows lines F1 and F4 along which the static pressure on the burner case is measured.

[FIGURE 5]

A schematic of station 3 is given in Fig. 6a. The axial component of the velocity (V_x) is measured in the combustion chamber, namely along the three transverse lines E1, E2, and E3. Figure 6a also shows the origin of the selected reference frame. The origin is on the nozzle and chamber centerline, and its X position is at the bottom of the combustion chamber.

All the measurements are repeated for two load conditions. One is that of full load when the throttling valve is fully open (condition V90). The other is the partial load regime, corresponding to a partial valve opening of 50° (condition V50). A schematic of the valve orientation for the two configurations is shown in Fig. 6b.

[FIGURE 6]

4 Computational fluid dynamics method

All numerical analyses are carried out with the commercial CFD code ANSYS FLUENT [22], using version v19.3, unless otherwise stated. The code is used to solve the pressure-based incompressible RANS equations. FLUENT uses the finite volume method for the space discretization of all conservation laws. In all analyses, a second-order upwind scheme for the convective fluxes is chosen. Diffusion terms are discretized with second-order finite-differencing. All simulations herein are time-dependent, and, all reported numerical results are time-averages of unsteady CFD simulations using a first-order discretization scheme in time with a dual time-stepping approach. None of the considered simulations could be performed using a steady-state solver, because, even if not large, the physical level of unsteadiness prevented convergence to a mean state to be achieved with a steady solver. All simulations use the COUPLED solver, which solves the continuity and momentum equations in a strongly coupled fashion, whereas all other transport equations are solved in a loosely coupled fashion.

Part of the presented analyses uses the $k-\omega$ SST turbulence model [16]. The model is based on Boussinesq hypothesis, and computes the turbulent viscosity μ_t from the turbulent kinetic energy k and the specific turbulence dissipation rate (ω), which are transported variables. The remainder of the analyses uses the higher-fidelity RSM approach [11].

RSM is a RANS approach that is not based on the Boussinesq hypothesis, and better accounts for the anisotropy of turbulence. Thus, it is often better suited for cases where this character is more pronounced, such as highly swirling flows [9, 23]. The independence of the Reynolds stress tensor τ_{ij} on the laminar stress tensor in the RSM approach, requires solving a transport equation for each of the six distinct components of τ_{ij}. Moreover, an additional transport equation for the dissipation of τ_{ij} needs to be solved. Therefore, RSM uses 7 transport equations to model turbulence. This increases notably computational costs with respect to two-equation turbulence models.

Several options are available for the equation of the τ_{ij} dissipation. These can be subdivided in ε-based methods, where ε is the turbulent dissipation rate, and ω-based methods. Two variants of each approach are implemented in FLUENT. The ε-based variants differ for how they model the pressure strain term in the τ_{ij} equations. The default option is that proposed by Gibson and Launder [24], Fu et al. [25], and Launder [26, 27]. This solution, named ”linear pressure strain term”, is less accurate than the ”quadratic pressure strain term” by Speziale, Sarkar, and Gatski [28], but is found to be more stable. The ε-based RSM variant tested in this study is the latter one; it has been found that, in order to prevent these simulations from becoming numerically unstable, the convection terms of the transport equations of τ_{ij} and ε have to be discretized with a first order upwind scheme.

The available ω-based RSM variants are the RSM-ω and the RSM-BSL variants. The RSM-ω model is based on the ω-equation of the standard $k-\omega$ model of Wilcox [12], which was shown to give free-stream sensitive results [29]. The RSM-BSL model uses instead the ω-equation of the baseline $k-\omega$ model of Menter [30], which removes the free-stream sensitivity. The ω-based RSM variant tested in this study is the latter one, which unlike the tested ε-based variant has been found to be sufficiently stable also with a second order upwind discretization of the convective terms of turbulence transport equations.

The RSM simulations are carried out with FLUENT version v21.2, as the use of v19.3 led to numerical instabilities causing residuals to rapidly grow, and the simulation to crash after just a few time steps.

5 Numerical set-up

5.1 Physical domain and grids.

The physical domain considered herein is shown in Fig. 7. It starts at the measurement station 1, it includes throttling valve, burner case and nozzle, and it contains the cylindrical combustion chamber. Preliminary analyses highlighted the necessity of resolving also the flow field around the combustion chamber to avoid strong numerical instabilities caused by recirculation regions reaching the outlet of the chamber. Thus, the physical domain extends $85d_c$ downstream of the chamber outlet, and $37.5d_c$ radially, as indicated in Fig. 7. Figure 7 shows the main outer boundaries of the physical domain, which include the primary inlet through which the fan feeds the burner, the secondary inlet through which air flowing past the combustion chamber enters the domain, the outlet boundary through which the primary and secondary air leave the domain, and the outer boundary. The BCs applied on these boundaries are stated in Section 5.2. The physical domain does not include the flame sensor, the spark plug and the bolts.

[FIGURE 7]

All meshes are generated with ANSYS FLUENT Meshing, and are high-quality hybrid unstructured grids with regular hexahedral cells in most of the domain. Polyhedral cells are used close to the boundaries, in regions connecting grid portions with different refinement, and where the complexity of the geometry requires their use. Figure 8 shows the longitudinal section of a grid with medium refinement for the V90 operating condition for simulations which resolve wall boundary layers (BLs) down to the wall without wall functions. As the number of cells increases significantly when solving BLs down to the wall, two different approaches have been assessed in this work. One reduces the computational cost by generating an inflation layer with only two cells in the direction normal to the walls. This method used wall functions (WFs). The other approach resolves BLs down to the wall. This is enabled by generating an inflation layer that guarantees a nondimensionalized wall distance y^+ of the cell centers closest to the walls smaller than 1 almost everywhere. For the fluid problem studied herein, the overall number of grid cells for the same level of grid refinement on the interior domain doubles when BLs are resolved. This method is labeled ”WR” in the remainder of this article. Section 7.1 will present a comparative analysis of the results obtained with the WR and WF.

[FIGURE 8]

5.2 Boundary Conditions

The BCs on the primary inlet boundary are prescribed as 2D maps of either total pressure or velocity. The two cases are labeled ”P” and ”V”, respectively. These maps are obtained elaborating the data measured at station 1.

The spatial variations of the measured total pressure at station 1 are relatively low. The maximum deviation from the mean of the five values measured at the five positions indicated by black dots in Fig. 4 is less than 2.5%. Including also the measured wall static pressure (white dots in Fig. 4) this difference increases to 16%. Since these variations are relatively small, and the highest differences arise in a narrow region close to the wall, the prescribed total pressure is based only on the measured points indicated in black. A constant interpolation method is used, whereby the total pressure on a point of the boundary, is the closest measured value. The result of this operation is shown in Fig. 9a, in the form of total pressure profiles extracted from the generated maps.

The spatial variations of the measured velocity in the primary inlet duct are more significant than those of the total pressure, with a maximum deviation from the mean above 15%. Moreover, the velocity decreases sharply near the walls, becoming zero there. Figure 9b shows the velocity profiles for the CFD simulations generated from the measured profiles. The CFD input values are interpolated along the lines $x_b = 0$ and $x_h = 0$ (Fig. 4) using a shape-preserving cubic Hermite interpolation. They are then extrapolated linearly to a distance from the wall of 20% of l_{x_b} and l_{x_h}, respectively. The profiles are then extended to the wall with the logarithmic law of the wall [31]. The 2D velocity map on the primary inlet boundary is obtained by interpolations based on the two profiles described above.

[FIGURE 9]

All wall boundaries, except the domain outer boundary, are treated as viscous walls. An inviscid wall condition is instead applied on the domain outer boundary (Fig. 7. A pressure outlet condition, which enforces zero gauge pressure, is enforced on the outlet boundary of the domain. To avoid the occurrence of back-flow on this boundary, a non-zero V_x of 0.002 m/s is on the secondary inlet boundary imposed secondary inlet boundary.

Choosing either of the aforementioned methods for prescribing the BC at the primary inlet, and either of the approaches described in Section 5.1 for handling wall BLs, four possible set-ups are defined, labeled ”P-WF”, ”P-WR”, ”V-WF”, and ”V-WR” in the parametric analyses of Section 7.1.

6 Mesh sensitivity analysis

Selected results of a three-mesh sensitivity study are presented in this section. Due to the high computational cost of these time-dependent simulations, the analysis is carried out only for the P-WF with $k-\omega$ SST model for the V90 operating condition. The limiting factor for the set-up choice is the computational cost of the fine grid simulation. The WF set-up was selected because the WR fine grid has a larger cell count of 17.43 million, and, more importantly, the convergence rate of the time-averaged flow field to a steady state was found to decrease when reducing the cell size in the near-wall regions. Both factors made the use of a fine grid without wall functions not affordable with the available computational resources. The reason for selecting the $k-\omega$ SST rather than an RSM set up, was also to make the computational burden of the fine grid simulation affordable.

The coarse, medium, and fine grids have, respectively, 3.8, 5.9, and 8.7 million cells. For reference, the WR grid with the same refinement of the medium WF grid away from walls has 12.0 million cells. Since the simulations are time-dependent, only the time-averaged flow fields computed with the three grids are compared. A constant time-step of $dt = 5 \cdot 10^{-3} s$ with 25 iterations at each time step are used in all simulations. The flow-through time, an estimate of the time required for a fluid particle to travel from the primary inlet boundary to the end of the combustion chamber, is defined as the ratio of a characteristic length and velocity. The characteristic length is defined as the sum of three lengths: the combustion chamber, the burner case and portion of the inlet duct included in the physical domain. The considered characteristic velocity is evaluated as the average measured velocity at station 1. All simulations are initialized with a hybrid initialization, and have been run for about 10 flow-through times in order to achieve a statistically stationary condition. From this time, simulations are run for another 50 flow-through times, and a time-average solution over this time interval is obtained at the end of the simulation. The solution sensitivity to mesh refinement is assessed by comparing local and global values of the mean flow field computed on the three grids. One considered parameter is the computed mass flow rate $\dot{m}_{air}$. Another parameter used for the analysis is the RMS of the differences between the local velocity V_x in a section A normal to the X axis and the mean velocity V_{b_c} in the same section. The definition of this global metric is:

$$RMS^A = \sqrt{\frac{\int_A (V_x - V_{b_c})^2 dA}{A}} \tag{1}$$

All velocities in Eq. (1) are final time-averaged values of the simulation, and, therefore, RMS^A provides only a measure of the spatial variability of the velocity, and not a measure of possible unsteady fluctuations.

The first, second and third rows of Tab. 2 report integral quantities computed on the coarse, medium and fine refinement grids, respectively. The second column provides the mass flow; the third, fourth and fifth columns provide the value of RMS^A, respectively, on the cross sections at the longitudinal positions where lines L1, L2, and E3 are positioned in Fig. 6a. One sees that the values of the mass flow rates are very similar in all three grids, and the three values are within about 0.4% of each other. The value sets of RMS^A at the three axial positions highlight that the differences between medium and fine grids are notably lower than those between the medium and the coarse grids in all cases. In fact, the RMS^A percentage differences between medium and fine grids lay between 0.8% and 1.9%, whereas those between coarse and medium grids range from 2.0% to 7.5%. These data provide a first indication of sufficient grid independence of the medium grid.

[TABLE 2]

The profiles of V_x computed on the lines L1, L2 and E3 are reported in Figures 10a, 10b and 10c, respectively. Figure 10b reports also the profiles of the radial velocity component V_r, which is significant at this position, due to the transverse jets in the conical nozzle. At all three positions, the profiles obtained with the medium and fine grids differ notably less than those obtained with the coarse and medium grids. On the line L2, the differences between coarse and medium profiles of V_r are particularly significant at $\frac{Y}{d_n} \approx \pm 0.3$, where the peaks of the radial velocity component due to the jets are observed. On line E3 in the combustion chamber, large differences between the coarse and medium profiles of V_x are also observed, despite the smaller flow gradients in this region.

[FIGURE 10]

Figure 11 compares the coarse, medium and fine grid wall pressure profiles on the line F1 indicated in Fig. 5. Consistently with the trends highlighted above, the fine and medium grid profiles are superimposed, whereas the coarse grid profile differs slightly from the other two for $\frac{X}{d_n} < -1.5$. That is the region where the flow from the primary inlet duct hits the facing wall of the burner case, causing static pressure to increase at this location.

[FIGURE 11]

The results above indicate the suitability of the medium refinement grid to properly resolve the flow physics of the considered industrial gas burner. As stated above, three wall BL resolving grids could not be used for the complete mesh sensitivity analysis, due to the computational burden of the fine grid analysis. However, the comparison of the results obtained with a BL-resolving 8.44 million-cell coarse grid and a 12.00-cell medium grid, not reported for brevity, showed relatively small differences of the two analyses, also in the near-wall regions. This occurrence gives confidence that also the medium level of refinement of WR set-up is adequate for the scopes of the reported analyses.

7 Results

The first part of this section presents a parametric analysis comparing a selection of results obtained with the numerical set-ups P-WF, P-WR, V-WF, and V-WR defined at the end of Section 5. In the second part, the solutions obtained with three turbulence models using the same wall BL approach and inlet BC type are compared. Finally, the detailed analysis of the flow field of the analyzed system is presented in the third subsection. The section also presents comparisons of the simulations with all available measured data.

7.1 CFD solution sensitivity to inlet BC and wall BLs resolution method

The $k-\omega$ SST turbulence model is used in all four numerical set-ups obtained by using either primary inlet BC and either wall BLs solution approach discussed in Section 5.

Figure 12a shows three sets of V_x profiles in the combustion chamber for the operating condition V90. The axial positions E1, E2, and E3 to which the profile sets refer are those indicated in Fig. 6a, and each set reports the CFD profiles computed with the four set-ups and the measured profile. The error bars on the experimental profiles are the RMSs of the deviations from the mean values of the measured time-series at each measurement point. The measurements at some locations were repeated, and the results are reported on the same plots. The left plot of Fig. 12a shows that, although the magnitude and position of the peak velocity are well predicted by P-WF, the shape of the profile differs from those predicted by the other three set-ups, which are closer to the measured data. This is a first indication of a poorer predictive performance of the P-WF set-up. At the axial positions E2 and E3, the Y position of the P-WF V_x peak is different from that of all other profiles (middle and right plots). Further investigations not reported for brevity show that a likely cause is that using wall functions to model part of the BL around the throttling valve results in a flow reversal where the valve has maximum thickness. This separation, not present when the BL is resolved down to the wall, affects the vortical patterns in the burner case and, subsequently, the V_x profiles in the combustion chamber. The flow reversal in the valve region is present also with the set-up V-WF. However, in the V-WF solution, its impact on the downstream flow is reduced due to the convective forces which, in the valve region, are higher than those of the P-WF flow field. This is because the velocities prescribed in set-up V-WF are higher than those computed with P-WF.

[FIGURE 12]

The P-WR, V-WR, and V-WF velocity profiles are close to each other. The only significant difference is seen in the left plot of Fig. 12a where the peak velocity is underpredicted by P-WR. The profiles predicted by the set-ups with prescribed velocity at the primary inlet differ very little, suggesting that the prediction improvements associated with resolving BLs for the V90 regime are small when the primary inlet velocity is prescribed.

Figure 12b refers to operating condition V50, and has the same structure as Fig. 12a. The P-WF set-up appears to perform better than in the V90 case, since its predictions are now closer to those of the other three set-ups and the experimental data. The left plot of Fig. 12b highlights that the profiles computed prescribing the inlet velocity differ significantly only in the central part of the profile, for $-0.4 < \frac{Y}{d_n} < 0.2$. Significant differences occur instead over most part of the profiles at stations E2 and E3 (middle and right plots). This suggests that these differences may be due primarily to differences in the flow field of the nozzle inlet duct. Thorough flow field investigations reveal that these differences occur in two regions: where the flow accelerates past the valve, and where it enters the nozzle inlet duct generating a recirculation region in the duct itself. These phenomena will be explained in detail in Section 7.3.

Table 3 reports the mass flow rate $\dot{m}_{air}$ estimated using the experimental data and the results of the P-WF and P-WR simulations for the two operating conditions. The $\dot{m}_{air}$ values computed by integrating the 2D velocity maps based on the measured velocities are reported in the Exp_{est} column. Those computed by the two CFD simulations are reported in the columns labeled P-WR and P-WF. The percentage differences of the $\dot{m}_{air}$ values of two simulations are reported in the Δ_{CFD} column. The P-WF estimates are between 5.4% and 6% larger than P-WR estimates. These notable differences underline the importance of using the more reliable wall BL resolving approach rather than wall functions to properly correlate mass flow rate and pressure jump. The values of $\dot{m}_{air}$ estimated from the measured velocities are consistently higher than those computed by CFD. This may be due to the uncertainty affecting the generation of the 2D velocity maps at the primary inlet.

[TABLE3]

The static pressure analyses below use the nondimensionalized pressure p^*, defined by Eq. (2).

$$p^* = \frac{p}{p_{t0}} \tag{2}$$

where p is the local static pressure and p_{t0} is a reference pressure corresponding to the total pressure at the center point of the primary inlet boundary. Both p and p_{t0} are gauge pressures. The measured values of p_{t0}, and those computed by the V-WR and V-WF set-ups are provided in Tab. 4 (the P-WR and P-WF set-ups enforce the measured p_{t0} value. Since in the V-WR and V-WF set-ups, p_{t0} is an output of the simulation, it provides an indication of the computed pressure jump when the velocities are prescribed at the primary inlet. The measured p_{t0} values are fairly reliable, as indicated by the fact that the Kimo manometer p_{t0} value regime V50 is $421.9 Pa$, very close to the value measured by the SDP816 transducer in Tab. 4.

[TABLE 4]

Figures 13a and 13b report the results obtained for the V90 regime on the lines F1 and F4, respectively, highlighted in

Fig. 5. Figure 13a shows that the trend of the P-WF profile differs slightly from that of the other three set-ups. The cause of this deviation is likely to be the same yielding the P-WF velocity patterns observed in Fig. 12a and discussed above. The profiles of p^* predicted by V-WF are lower than those predicted by the other three set-ups, but the slope of this profile is similar to that of the P-WR and V-WR profiles. Figure 13b underlines that the V-WF profile on line F4 is lower than the other three numerical profiles. The results obtained for the V50 regime, not reported for brevity, show that all CFD profiles are very close to each other.

[FIGURE 13]

Finally, Tab. 5 reports the values of p^* evaluated in the fuel box (FB in Fig. 5) for all considered cases. The value of p^*_{FB} measured with the Kimo transducer for the V50 condition is -0.069. V-WR and P-WR seem to perform slightly better than V-WF and P-WF, even though the differences are minimal. This may suggest that resolving wall BLs has a stronger impact on the nondimensionalized static pressure predicted in the fuel box than the choice of the quantity prescribed at the primary inlet.

[TABLE 5]

The results shown in this section indicate that P-WF gives poorer predictions in full load conditions, while V-WR overestimates velocity magnitudes in partial load conditions. Thus, P-WR has been chosen as baseline set-up for the remainder of the analyses, as it gives good predictions in both operating conditions and is more trustworthy than V-WF which does not resolve BLs.

7.2 CFD solution sensitivity to turbulence model.

This section presents a parametric study on the impact of using either the SST or the RSM turbulence model in the P-WR analysis of the considered problem.

Figures 14a and 14b, featuring the same structure of Figures 12a and 12b, report the V_x profiles on in the combustion chamber for operating conditions V90 and V50, respectively, using the considered turbulence models. At design conditions (Fig. 14a), the two RSM set-ups predict very similar velocity profiles. The RSM set-ups yield slightly better prediction than the $k-\omega$ SST, especially in the region close to the nozzle exit (line E1). Some larger differences between the two RSM set-ups occur for the V50 condition Fig. 14b). The RSM-BSL model predicts the position of the peak velocity and the overall shape of the distribution better than both the SST and RSM-ε. The latter two models, however, yield a better prediction of the peak velocity magnitude on the E1 line. The $k-\omega$ SST model performs slightly worst than the RSM variants, especially in the V90 condition, where the values of V_x that it predicts close to the nozzle exit are too low with respect to measurement (left plot of Fig. 14a).

[FIGURE 14]

The comparison of the p^* profiles on the F1 and F4 lines, not reported for brevity, does not show significant differences among the predictions using the three turbulence models.

Table 6 provides the values of p^* in the fuel box. One sees that all models succeed in predicting a small negative gauge pressure, differing from the experimental value by less than 1% of p_{t0} for the $k-\omega$ SST and RSM-BSL set-ups. The RSM-ε model underestimates the magnitude of the FB gauge pressure, particularly at design conditions. A possible cause may be the use of a first order discretization for the convective terms in the τ_{ij} and ε equations, as discussed in Section 4. Overall, all turbulence models perform fairly well for the V50 condition, although the RSM predictions are closer to the experimental measurement than the $k-\omega$ SST model. The p^* value recorded by the Kimo manometer for the V50 regime is -0.069, slightly different from the reading of that SDP816 transducer, and very close to the RSM-BSL prediction.

[TABLE 6]

The comparative analysis above highlights that, overall, the RSM-BSL set-up yields prediction improvements over the $k-\omega$ SST and the RSM-ε set-ups. Therefore, the RSM-BSL method is used in the detailed flow analyses presented below.

7.3 Flow field analyses

In the analyses below, the P-WR RSM-BSL set-up is used to investigate the key flow features of the gas burner for both V90 and V50 operating conditions.

7.3.1 Flow field at design conditions

Figure 15 shows the flow field in the burner case at the design conditions V90. As the valve is parallel to the direction of the oncoming flow, the air stream flows around the valve without flow reversals. However, separation occurs downstream, due to the backward facing steps at the junction of the inlet duct and the burner case. The resulting vortical structures are visible in all three subplots of Fig. 15b. The recirculation zone labeled "A_1" covers the whole width of the burner case. The fuel duct and plate, highlighted in by solid and dashed rectangles, respectively, in Fig. 15b, and visible more clearly in Fig. 2a, interact with the counter-rotating vortex in the upper region of the case, breaking it into two weaker vortices labeled "B_1" and "B_2". The three plots of Fig. 15b are similar to each other, and show that the velocity gradients in the X direction are small in this region. In the region highlighted by the rectangle in Fig. 15a, one sees that the fluid accelerates entering the nozzle inlet duct. A recirculation region is formed on the inner wall of the nozzle inlet duct opposite the direction of the oncoming flow.

[FIGURE 15]

Figure 16 reports the velocity field in the YZ planes whose X positions are indicated in Fig. 15a. In all three planes, the asymmetry of the V_x contour maps of the flow approaching the nozzle from outside the fuel duct is visible. Flow asymmetry exists also in the nozzle inlet duct, as clearly visible in Fig. 16a. The reduction of V_x in the Y direction indicates that most of the flow rate goes through the half of the burner case at $Y<0$. This effect is particularly significant at the section closer to the inlet duct (left plot). Figure 16 also illustrates the downstream development of the vortices identified in Fig. 15b. The strongest vortex "A_1" dominates the flow in the burner case. The vortex "B_2" is completely dissipated, as it is no longer visible in Fig. 16b. The vortex ”B_1” does not disappear completely, but its intensity decreases significantly as the stream advances in the burner case.

[FIGURE 16]

The velocity field of the nozzle is analyzed in Fig. 17. A fast stream on the centerline, originating from the nozzle inlet duct, is visible in Fig. 17a. The velocity contour map also highlights the asymmetry of this primary stream. High-speed secondary streams or jets emanate from the holes on the nozzle cone, and merge with the primary stream. Figures 17b and 17c show the flow patterns before and after the nozzle. One can see that the vortex ”A_1” generated upstream is still significant at the inlet of the combustion chamber.

[FIGURE 17]

Figure 18 shows the contour plot of p^* in the plane $Z = 0$ of the burner case. The figure shows a stagnation region (highlighted by a rectangle) resulting from the impingement of the oncoming flow entering the case from the inlet duct.

[FIGURE 18]

Computed and measured p^* profiles on lines F1 and F4 are compared in Figures 19a and 19b, respectively. On line F1, both experiments and simulations predict higher static pressure in front of the inlet duct ($\frac{X}{d_n} < -1.5$) than immediately downstream ($\frac{X}{d_n} > -1.5$). This higher pressure is caused by the impingement of the oncoming primary flow on the wall of the burner case. On line F4 (Fig. 19b), both simulations and experiments show that p^* is almost constant, and a small adverse pressure gradient exists. Both plots of Fig. 19 show that the level of static pressure in the burner case is overpredicted by CFD. This implies that the pressure drop in the inlet duct and past the valve is underestimated by CFD. This could be due to the fact that the computed velocity field on the primary inlet boundary does not feature transverse velocity components, and, therefore, does not take into account all the expected three-dimensionality of the flow coming from the fan.

[FIGURE 19]

Measured and computed profiles of the V_x velocity component on lines E1, E2, and E3 are compared in Fig. 20. Inspection of these profiles indicates that the lack of axial symmetry in the burner case and around the nozzle extends to the combustion chamber. The measured profiles of all plots of Fig. 20 show that the peak velocity is shifted towards positive Y values, and this pattern is correctly predicted by the CFD simulation. The asymmetry is due to the highly 3D flow field in the burner case, caused primarily by the 90^o turn when the primary stream enters the burner case. Computed velocity profiles close to the nozzle (left and middle plots) are in good agreement with experiments both in terms of peak velocity and shape of the profile. Further downstream (right plot) the computed V_x profile is slightly higher than the measured profile, although the overall agreement remains fairly good.

[FIGURE 20]

7.3.2 Flow field at off-design conditions

Figure 21 presents the velocity field in the burner case for the off-design regime V50. As highlighted in Fig. 21a, the direction of the longer axis of the valve cross section forms an angle of 40^o with the oncoming flow direction. Due to this high flow incidence to the valve, a low-speed recirculating flow region forms behind the valve. A second flow feature caused by this orientation of the valve is an acceleration of the two streams flowing on the two sides of the valve. These high velocity streams are highlighted with ellipses. The stream highlighted by the lower ellipse reaches directly the nozzle inlet duct in the region indicated by a rectangle. When this stream hits the inlet area of the nozzle duct, a separation bubble forms on the inner wall of the duct facing the oncoming stream, similarly to the V90 operating condition. Figure 21b shows the presence of two secondary flows in the Z direction at the end of the inlet duct, highlighted by dashed oriented curves in the central plot. These secondary flows are due primarily to the two forward-facing steps located at the top and bottom of the inlet duct, indicated by circles in all three subplots. To a minor extent, vortices A_1 and B_1 also contribute to the formation of these secondary flows, by pushing the flow toward the center of the inlet duct. The point where the two secondary flows meet is marked by a solid circle in Fig. 21a. This flow feature also exists at the design condition V90, but, due to the greater momentum of the flow in the Y direction following the valve (i.e. larger V_y level), it is less pronounced. This can be seen by comparing Figures 15b and 21b. The comparison also highlights that the velocity variations in the X direction, in this region of the burner case, are stronger in the V50 condition. Figure 21b also shows the presence of two secondary vortices, "A_0" and "B_0", which are not observed at design conditions. These vortices are not convected downstream: they are visible in the top subplot of Fig. 15b, and by the time the flow reaches the section at $X = X_3$, they are no longer visible.

[FIGURE 21]

The three subplots of Fig. 22 examine the velocity field at the axial stations X_4, X_5 and X_6 indicated in Fig. 21a. The behavior of the flow in this region is similar to that of the V90 regime considered in Fig. 16, with some differences. For example, the interaction of vortices A_1 and B_1, which have different relative strenghts with respect to the design condition, lead to the formation of a small secondary vortex B_3 at station X_5, not observed in the V90 operating condition.

[FIGURE 22]

The flow field in the nozzle is visualized in Fig. 23. The overall velocity level is in the V90 condition. Figure 23c also shows that the vortex A_1 persists in the combustion chamber, similarly to the design condition.

[FIGURE 23]

Figure 24 compares CFD and measured p^* profiles along lines F1 and F4, and its inspection leads to similar considerations to those reported in Section 7.3.1 for the V90 condition. For the V50 operating condition, two sets of measured static pressure are available, one measured with the SDP816-500PA analog transducer (Exp-SDP816 in the legend) and one measured with the Kimo MP 200 P manometer (Exp-Kimo in the legend). In this operating condition $p_{t0} = 424.7$Pa for SDP816 and CFD, while $p_{t0} = 421.9$Pa for Kimo. Figure 24 shows that the two transducers give very similar readings. The simulation predicts a peak static pressure at $-2 < \frac{X}{d_n} < -1.5$ not seen in the experimental data. The CFD peak occurs at the position where the stream highlighted by the ellipse below in Fig. 21a hits the wall of the burner case. Possible reasons for this mismatch could be that the position and size of the high pressure region may depend on seemingly minor geometric features not included in the physical domain. Moreover, the distribution of the pressure taps may be too coarse to resolve this pressure variation. Both the computed and measured pressure profiles on line F4 (Fig. 24b shows that the adverse pressure gradient in the streamwise direction is stronger than that observed in Fig. 19b for the V90 operating condition. The magnitude of the predicted and computed pressure gradient is in good agreement.

[FIGURE 24]

Measured and computed V_x profiles in the combustion chamber are compared in Fig. 25. An overall good agreement of experimental measurements and numerical results is observed. At the axial position E1 (left plot) close to the nozzle, a fairly good agreement is observed, with some discrepancies arising only in the region around the centerline ($Y/d_n = 0$), where the numerical model overpredicts the measured V_x profile. The agreement improves further moving downstream, as visible in the middle and right plots, comparing measurements and simulations at positions E2 and E3, respectively. Comparing the three subplots of Fig. 25 to those of the V90 regime reported in Fig. 20, highlights that also in the V50 condition all V_x profiles have a positive Y offset, indicating a lack of axial symmetry of the flow in the combustion chamber.

[FIGURE 25]

8 Conclusions

The main features of the cold flow physics of a non-premixed industrial gas burner at full and partial load have been investigated by means of RANS CFD, and flow measurements taken in a full scale test rig have been used for CFD validation. Parametric CFD analyses aiming at assessing the impact on the computed solution of $a)$ inflow BC type (imposed velocity map or total pressure), $b)$ resolution of wall-bounded flows (wall functions or integration down to walls), and $c)$ turbulence closure ($k-\omega$ SST, RSM-BSL or RSM-ε models) have been carried out.

At both operating conditions, the flow field is dominated by highly 3D flow phenomena, including: $a)$ a strong deviation of the flow field in the burner case until downstream of the nozzle exit from the axisymmetric pattern, due to a 90° turn of the flow between the air admission duct and the burner, $b)$ a system of large secondary vortices caused by the abrupt change in cross sectional area at the end of the air inlet duct, $c)$ a separation bubble at the beginning of the nozzle inlet duct, due to the flow arriving from the air admission duct being orthogonal to the nozzle inlet duct, and $d)$ flow recirculaton pockets caused by forward and backward facing steps on the inner walls of the entire system. In the partial load condition, the overall flow field pattern is made more complex also by the stalled flow pocket around the admission valve, and the two air jets between the valve ends and its bounding walls.

Overall good agreement of CFD results and experimental data has been observed at both operating conditions using the RSM-BSL turbulence model with imposed total pressure at the inlet of the air admission duct, and integration of the governing equations down to the wall to resolve the near-wall flows.

The analysis of the solution sensitivity to the resolution of the wall bounded flows and the inflow BC type, carried out using the $k-\omega$ SST model, show that, at the full load operating condition, the largest deviations from the measured data are observed when using wall functions and imposing the inlet total pressure. At the partial load condition, the four solutions are relatively close to each other and in fairly good agreement with measured data.

Comparative analyses of the four solutions of the full load condition, indicate that the deviation of the solution with imposed inlet pressure and using wall functions from the other three solutions may be due to both the inadequacy of the wall function approach to handle flow separation, and the sensitivity of the velocity field to local flow separations being larger when imposing the total pressure rather than the velocity at the inlet of the air admission duct. s the observed flow separations occur only in localized regions, one could refine the near-wall grid and resolve BLs only in separated flow regions, and use wall functions elsewhere. This hybrid set-up would enable achieving reduced computational costs and overall adequate solution fidelity.

The improvement of the agreement of simulations and measurements obtained by using RSM may not seem sufficiently large to justify its increased computational cost over that of two-equation eddy viscosity models. However, available literature shows that RSM is better suited than eddy viscosity models to predicting turbulent diffusion flames. This holds also for gas burners notably simpler than the industrial gas burner considered herein, for example purely cylindrical combustors with fuel and oxidizer forming two coaxial non-swirling flows [8, 32]. Therefore, the RSM-BSL closure is deemed to be a well suited method for the follow-on analysis of the reactive flow of the considered burner. Nevertheless, burner design studies have also highlighted the potential benefits that optimizing certain burner flow patterns may have on improving combustion efficiency and reducing pollutants [33, 34]. In design optimization, which typically requires analyzing a large number of system variants, computationally more affordable eddy viscosity RANS set-ups also play an important role in the initial phase of burner design optimization.

Acknowledgements

This project is supported by the Center for Global Eco-Innovation, the European Regional Development Fund, and Proctor Process Plant, which designed and manufactured the industrial burner. All the simulations in this work were run on the Lancaster University High End Computing (HEC) cluster. The authors are grateful to the Reviewers for their helpful comments, and the Editors for handling the article submission.

References

[1] Barlow, R., and Frank, J., 1998. "Effects of turbulence on species mass fractions in methane/air jet flames". *Symposium (International) on Combustion,* **27**(1), pp. 1087–1095.

[2] Barlow, R., Frank, J., Karpetis, A., and Chen, J.-Y., 2005. "Piloted methane/air jet flames: Transport effects and aspects of scalar structure". *Combustion and Flame,* **143**(4), pp. 433–449.

[3] Schneider, C., Dreizler, A., Janicka, J., and Hassel, E., 2003. "Flow field measurements of stable and locally extinguishing hydrocarbon-fuelled jet flames". *Combustion and Flame,* **135**(1), pp. 185–190.

[4] Lysenko, D., Ertesvåg, I., and Rian, K. E., 2014. "Numerical Simulations of the Sandia Flame D Using the Eddy Dissipation Concept". *Flow Turbulence and Combustion,* **93**, p. 7665.687.

[5] Saini, R., Prakash, S., De, A., and Yadav, R., 2018. "Investigation of NOx in piloted stabilized methane-air diffusion flames using finite-rate and infinitely-fast chemistry based combustion models". *Thermal Science and Engineering Progress,* **5**, pp. 144–157.

[6] Pitsch, H., and Steiner, H., 2000. "Scalar mixing and dissipation rate in large-eddy simulations of non-premixed turbulent combustion". *Proceedings of the Combustion Institute,* **28**(1), pp. 41–49.

[7] Pecquery, F., Moureau, V., Lartigue, G., Vervisch, L., and Roux, A., 2014. "Modelling nitrogen oxide emissions in turbulent flames with air dilution: Application to LES of a non-premixed jet-flame". *Combustion and Flame,* **161**(2), pp. 496–509.

[8] He, D., Yu, Y., Kuang, Y., and Wang, C., 2021. "Model Comparisons of Flow and Chemical Kinetic Mechanisms for Methane–Air Combustion for Engineering Applications". *Applied Sciences,* **11**(9).

[9] Wronski, T., Schönnenbeck, C., Zouaoui-Mahzoul, N., Brillard, A., and Brilhac, J.-F., 2022. "Numerical simulation through Fluent of a cold, confined and swirling airflow in a combustion chamber". *European Journal of Mechanics - B/Fluids,* **96**, pp. 173–187.

[10] Launder, B. E. B. E., 1972. *Lectures in mathematical models of turbulence / B. E. Launder and D. B. Spalding.* Academic Press, London.

[11] Launder, B. E., Reece, G. J., and Rodi, W., 1975. "Progress in the development of a Reynolds-stress turbulence closure". *Journal of Fluid Mechanics,* **68**(3), p. 537–566.

[12] Wilcox, D. C., et al., 1998. *Turbulence modeling for CFD*, Vol. 2. DCW industries La Canada, CA.

[13] Meraner, C., Li, T., Ditaranto, M., and Løvås, T., 2018. "Cold flow characteristics of a novel bluff body hydrogen burner, journal = International Journal of Hydrogen Energy". pp. 7155–7168.

[14] Dutka, M., Ditaranto, M., and Løvås, T., 2016. "NOx emissions and turbulent flow field in a partially premixed bluff body burner with CH4 and H2 fuels". *International Journal of Hydrogen Energy,* **41**(28), pp. 12397–12410.

[15] Shih, T.-H., Liou, W. W., Shabbir, A., Yang, Z., and Zhu, J., 1995. "A new $k-\varepsilon$ eddy viscosity model for high reynolds number turbulent flows". *Computers & Fluids,* **24**(3), pp. 227–238.

[16] Menter, F., Kuntz, M., and Langtry, R., 2003. "Ten years of industrial experience with the SST turbulence model". *Heat and Mass Transfer,* **4**, 01.

[17] Menter, F. R., 2015. "Best practice: scale-resolving simulations in ANSYS CFD". *ANSYS Inc.:Canonsburg, PA, USA,* **1**.

[18] Menter, F., 2018. "Stress-Blended Eddy Simulation (SBES)—A New Paradigm in Hybrid RANS-LES Modeling". In Progress in Hybrid RANS-LES Modelling, Y. Hoarau, S.-H. Peng, D. Schwamborn, and A. Revell, eds., Springer International Publishing, pp. 27–37.

[19] Sensirion, 2018. SDP8xx-Analog datasheet. `https://www.mouser.co.uk/datasheet/2/682/SERI_S_A0004817208_1-2524897.pdf`. Accessed on 03 October 2022.

[20] Kimo-Ltd. Kimo MP 200 P Thermo Anemometer Manometer datasheet. `https://www.netzerotools.com/assets/images/pdfs/kimo/mp200/NZ-kimo-MP200-manometer-datasheet.pdf`. Accessed on 03 October 2022.

[21] TSI-Inc, 2014. TA440 thermal anemometer datasheet. `https://tsi.com/getmedia/fd36afb0-67d4-4cf5-a517-cc3743024329/TA410-TA430-440_Thermal_Anemometers_A4_UK_2980548-web?ext=.pdf`. Accessed on 03 October 2022.

[22] Ansys-Inc, 2019. Fluent theory guide, release 2019.r3. `https://www.ansys.com/Products/Fluids/ANSYS-Fluent`. Accessed on 11 May 2022.

[23] Morrall, A., Quayle, S., and Campobasso, M., 2020. "Turbulence modelling for RANS CFD analyses of multi-nozzle annular jet pump swirling flows". *International Journal of Heat and Fluid Flow,* **85**, p. 108652.

[24] Gibson, M. M., and Launder, B. E., 1978. "Ground effects on pressure fluctuations in the atmospheric boundary layer". *Journal of Fluid Mechanics,* **86**(3), p. 491–511.

[25] Fu, S., Launder, B., and Leschziner, M., 1987. "Modelling strongly swirling recirculating jet flow with Reynolds-stress transport closures". In 6th Symposium on Turbulent Shear Flows, pp. 17_6_1–17_6_6.

[26] Launder, B., 1989. "Second-Moment closure and its use in modelling turbulent industrial flows". *International Journal for Numerical Methods in Fluids,* **9**, pp. 963–985.

[27] Launder, B., 1989. "Second-moment closure: present… and future?". *International Journal of Heat and Fluid Flow,* **10**, pp. 282–300.

[28] Speziale, C. G., Sarkar, S., and Gatski, T. B., 1991. "Modelling the pressure–strain correlation of turbulence: an invariant dynamical systems approach". *Journal of Fluid Mechanics,* **227**, p. 245–272.

[29] Menter, F. R., 2009. "Review of the shear-stress transport turbulence model experience from an industrial perspective". *International journal of computational fluid dynamics,* **23**(4), pp. 305–316.

[30] Menter, F. R., 1994. "Two-equation eddy-viscosity turbulence models for engineering applications". *AIAA journal,* **32**(8), pp. 1598–1605.

[31] von Kármán, T., 1931. "Mechanical similitude and turbulence". NACA, Washington, DC,USA.

[32] Snegirev, A., and Frolov, A., 2011. "The large eddy simulation of a turbulent diffusion flame". *High Temperature,* **49**, 10, pp. 690–703.

[33] Zhang, Y., Xing, Y., and Chen, S., 2018. "CFD investigation based on gas burner with low-NOx strategy of fuel-staging". *IOP Conference Series: Earth and Environmental Science,* **153**(3), may, p. 032022.

[34] Du, H., Li, Z., Liu, Z., Zhang, M., Chen, Z., Song, J., Fang, F., and Xiao, R., 2022. "Influence of the Parallel C-Layer Secondary Air on Flow, Combustion and NOx Generation Characteristics of a 600mwe FW Down-Fired Boiler Retrofitted with a Stable Combustion Organization Mode". *Combustion Science and Technology,* **0**(0), pp. 1–25.

List of Tables

List of Figures

Table 1: Dimensions of primary inlet duct, gas burner, and combustion chamber normalized by nozzle external diameter d_n.

l_n/d_n	l_b/d_n	h_b/d_n	l_{in}/d_n	l_{x_b}/d_n	l_{x_h}/d_n	l_c/d_n	d_c/d_n
1.00	2.48	1.36	6.40	0.66	0.80	16.00	6.40

Table 2: Mass flow rates and velocity RMS^A values on cross sections at positions L1, L2 and E3 computed with coarse, medium and fine grid $k-\omega$ SST P-WF set-up for operating condition V90.

Load Condition	$\dot{m}_{air}[\frac{kg}{s}]$	$RMS^A_{L1}[\frac{m}{s}]$	$RMS^A_{L2}[\frac{m}{s}]$	$RMS^A_{E3}[\frac{m}{s}]$
Coarse	$6.310 \cdot 10^{-2}$	2.971	1.022	0.895
Medium	$6.334 \cdot 10^{-2}$	3.210	1.043	0.980
Fine	$6.333 \cdot 10^{-2}$	3.269	1.052	0.993

Table 3: Air mass flow rate estimated experimentally from the measured velocities and computed by the CFD prescribing the inlet total pressure for the V90 and V50 operating conditions

Load Condition	$\dot{m}_{air}[\frac{Kg}{s}]$			$\Delta_{CFD}[\%]$
	Exp_{est}	P-WR	P-WF	
V90	$6.95 \cdot 10^{-2}$	$5.97 \cdot 10^{-2}$	$6.33 \cdot 10^{-2}$	6.0
V50	$5.79 \cdot 10^{-2}$	$5.33 \cdot 10^{-2}$	$5.62 \cdot 10^{-2}$	5.4

Table 4: Reference pressures measured and computed by the CFD prescribing the inlet velocities for the V90 and V50 operating conditions.

Load Condition	$p_{t0}[Pa]$		
	Exp-SDP816	V-WR	V-WF
V90	356.5	486.7	444.7
V50	424.7	515.5	464.5

Table 5: Nondimensionalized static pressure p^* in the fuel inlet box evaluated with different set-ups for V90 and V50 conditions

Load Condition	$p^*_{FB}[-]$				
	Exp-SDP816	V-WR	V-WF	P-WR	P-WF
V90	-0.107	-0.111	-0.121	-0.111	-0.120
V50	-0.062	-0.070	-0.077	-0.072	-0.080

Table 6: Nondimensionalized static pressure p^* in the fuel inlet box measured and evaluated with different turbulence models for V90 and V50 conditions

Load Condition	$p^*_{FB}[-]$			
	Exp-SDP816	k-ω SST	RSM-BSL	RSM-ε
V90	−0.107	−0.111	−0.102	−0.082
V50	−0.062	−0.072	−0.069	−0.059

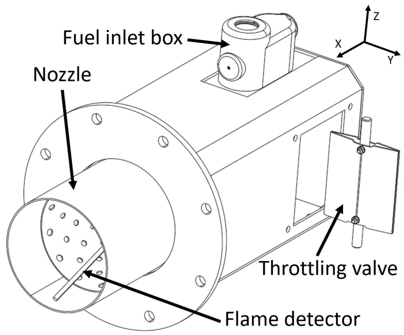

(a) Burner outer geometry.

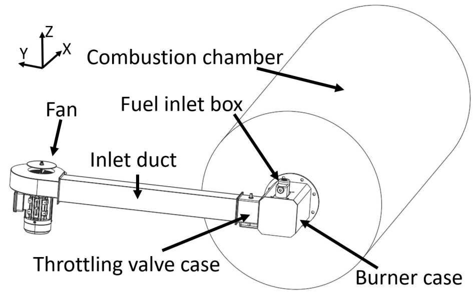

(b) Whole system view.

Fig. 1: Studied gas burner.

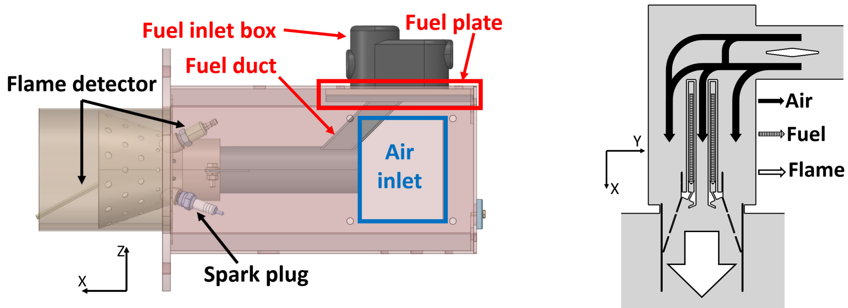

(a) Translucent longitudinal view. (b) Flow path schematic.

Fig. 2: Inner views of gas burner.

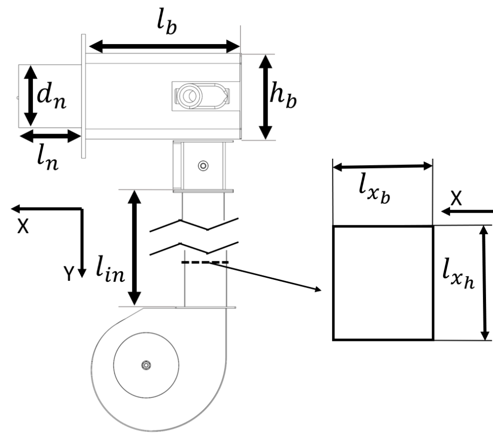

Fig. 3: Geometry parameters of primary inlet duct and gas burner.

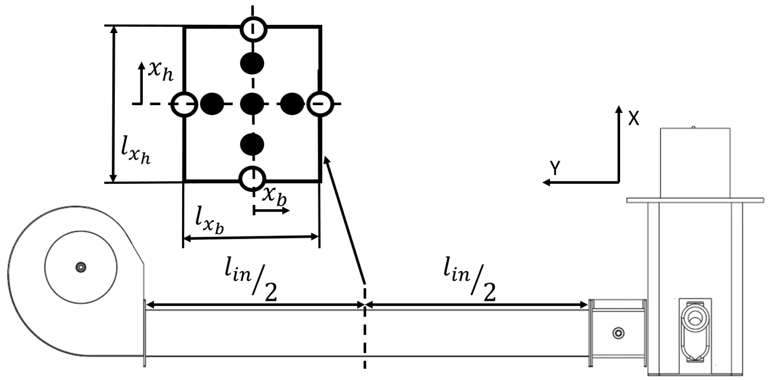

Fig. 4: Schematic of station 1.

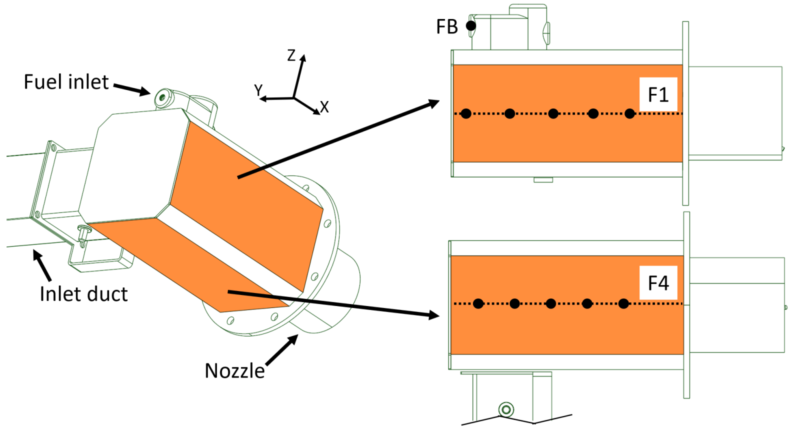

Fig. 5: Schematic of station 2. Black dots indicate pressure tap positions.

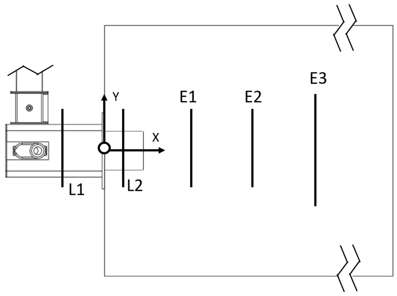

(a) Longitudinal positions of velocity traverses.

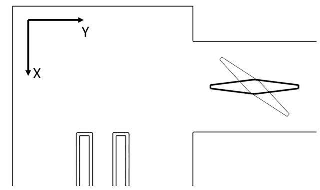

(b) Valve position at full load operation V90 (thick line), and partial load operation V50 (thin line).

Fig. 6: Schematic of station 3, and valve regulation.

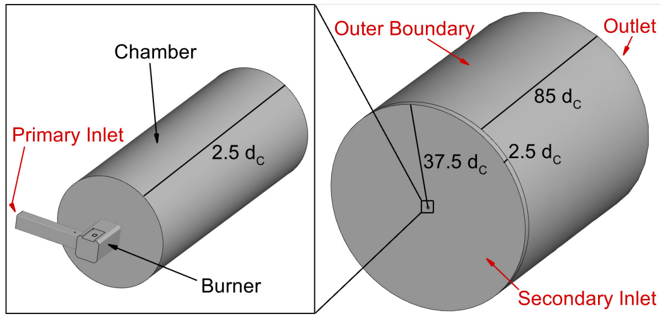

Fig. 7: Main dimensions and outer boundaries of physical domain.

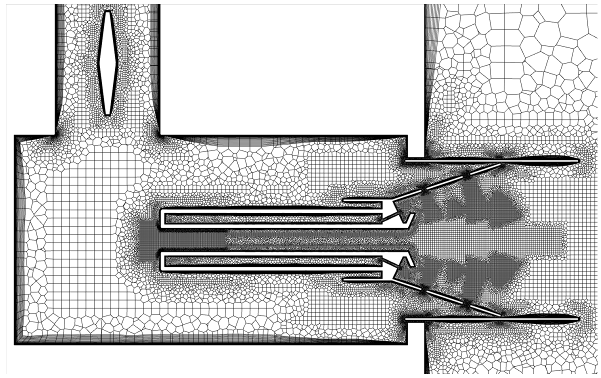

Fig. 8: Longitudinal section of medium refinement grid for analysis of V90 operating condition resolving boundary layers down to wall.

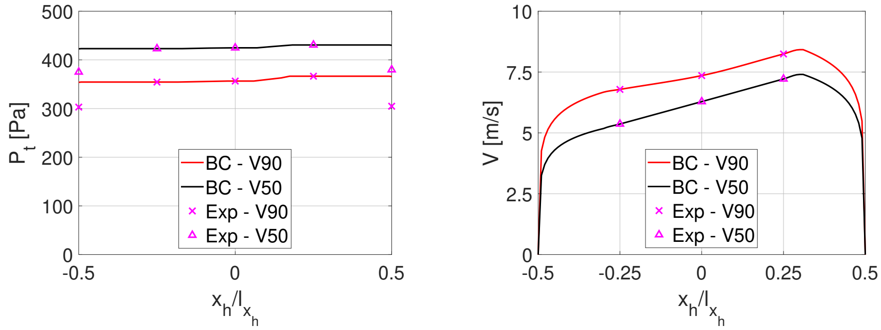

(a) Total pressure profiles.

(b) Velocity profiles.

Fig. 9: Measurement-based data for primary inlet boundary conditions at V90 and V50 conditions.

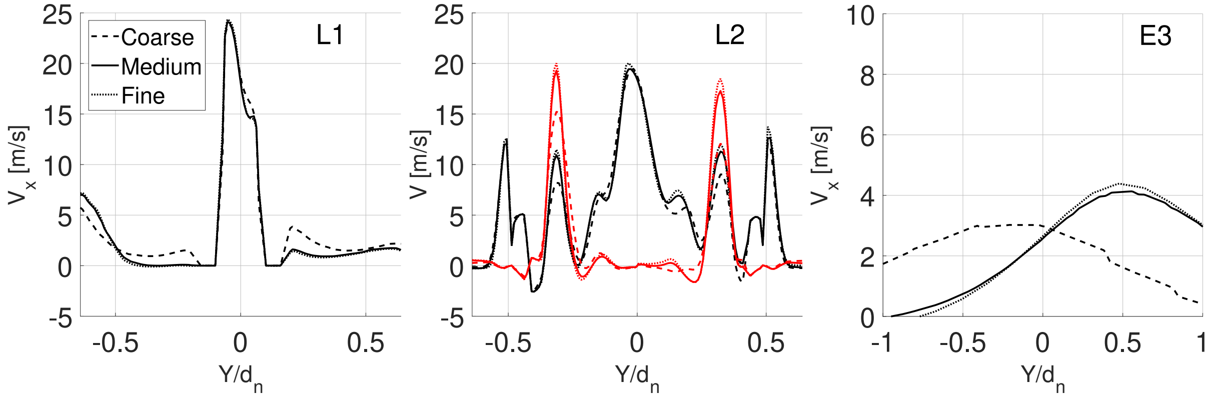

(a) Profiles of V_x on line L1.

(b) Profiles of V_x (black) and V_r (red) on line L2.

(c) Profiles of V_x on line E3.

Fig. 10: Profiles of V_x velocity components on transversal lines L1, L2 and E3 computed with coarse, medium and fine grid $k-\omega$ SST P-WF set-up for operating condition V90. Middle subplot also reports profiles of V_r velocity component.

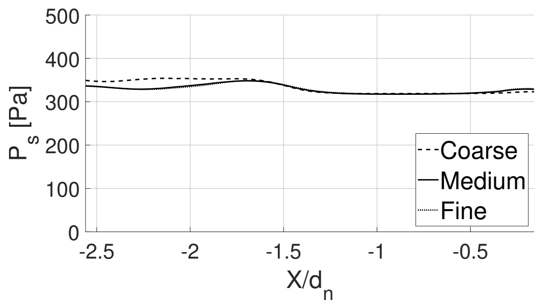

Fig. 11: Wall pressure profiles on lines F1 computed with coarse, medium and fine grid $k-\omega$ SST P-WF set-up for operating condition V90.

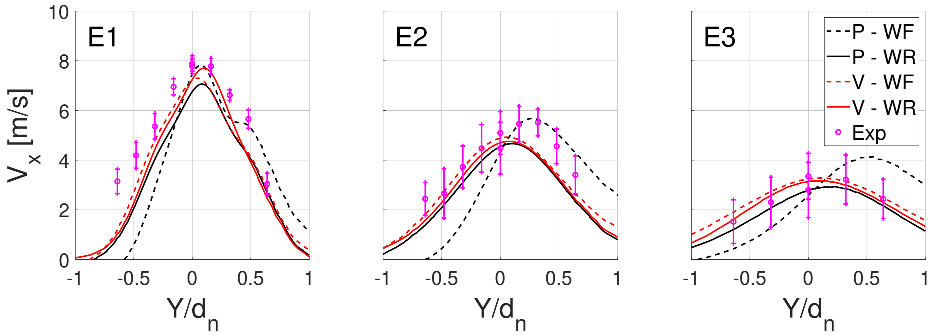

(a) V90 operating condition.

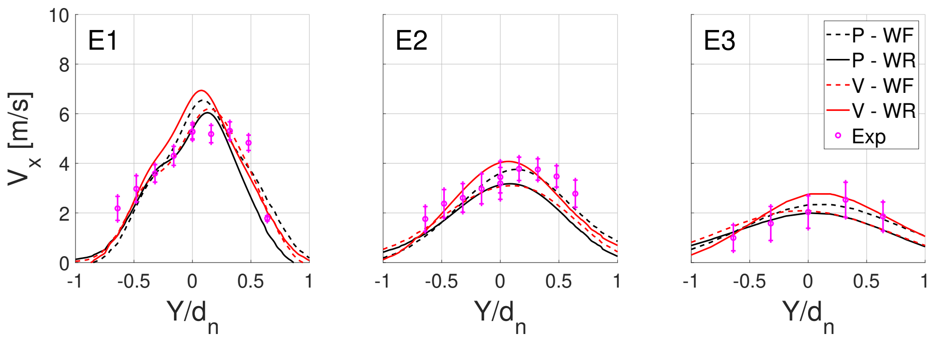

(b) V50 operating condition.

Fig. 12: Analysis of solution sensitivity to inlet boundary conditions and wall BL modeling: computed and measured V_x profiles on transversal lines E1, E2, and E3 in combustion chamber.

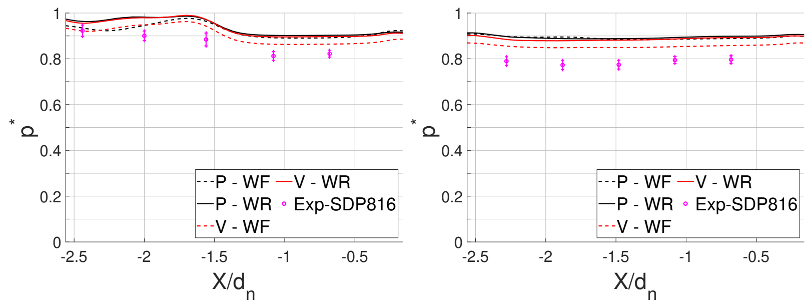

(a) Profiles on line F1.

(b) Profiles on line F4.

Fig. 13: Analysis of solution sensitivity to inlet boundary conditions and wall BL modeling: computed and measured nondimensionalized static pressure at V90 condition.

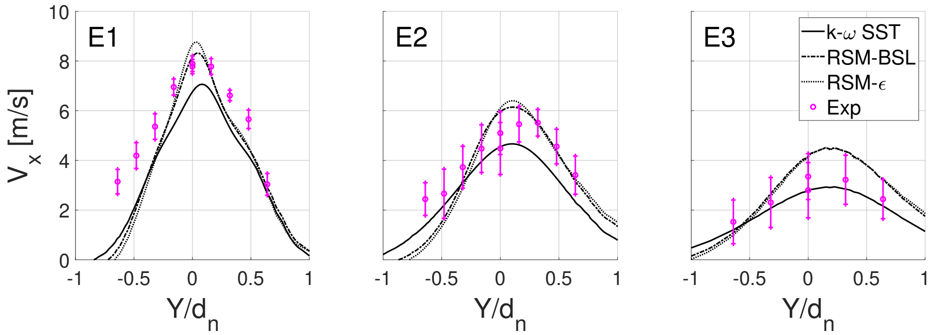

(a) V90 operating condition.

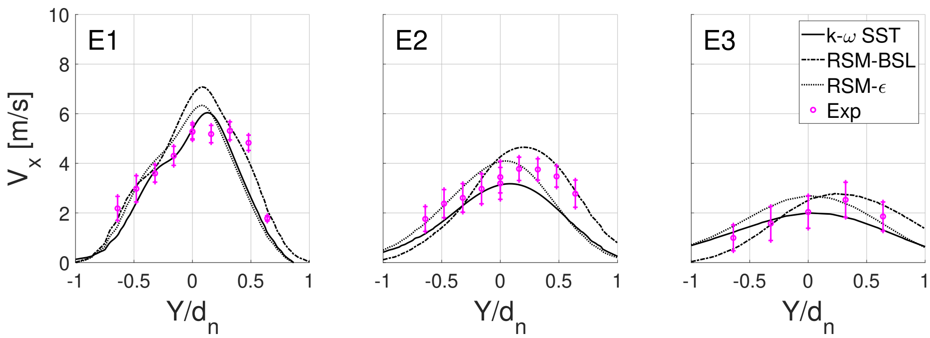

(b) V50 operating condition.

Fig. 14: Analysis of solution sensitivity to turbulence model: computed and measured V_x profiles on transversal lines E1, E2, and E3 in combustion chamber.

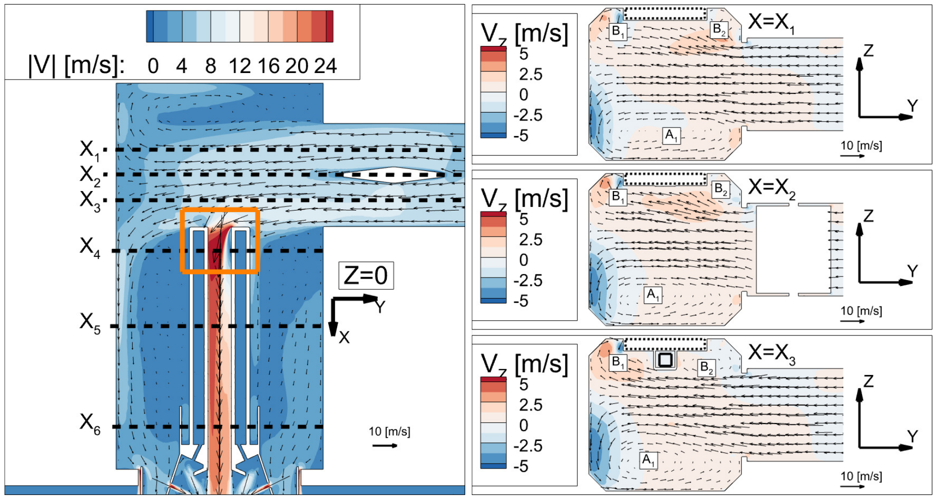

(a) (b)

Fig. 15: Velocity field in burner case at V90 condition computed with RSM-BSL P-WR.

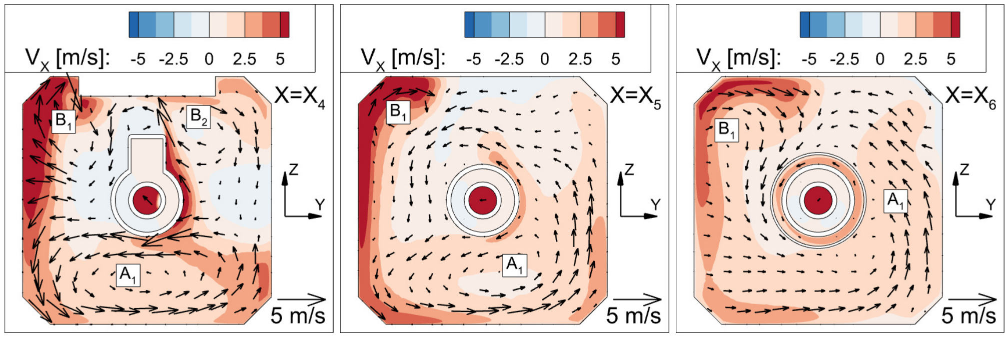

(a) Section X4. (b) Section X5. (c) Section X6.

Fig. 16: Velocity field in downstream part of burner case at V90 condition computed with RSM-BSL P-WR.

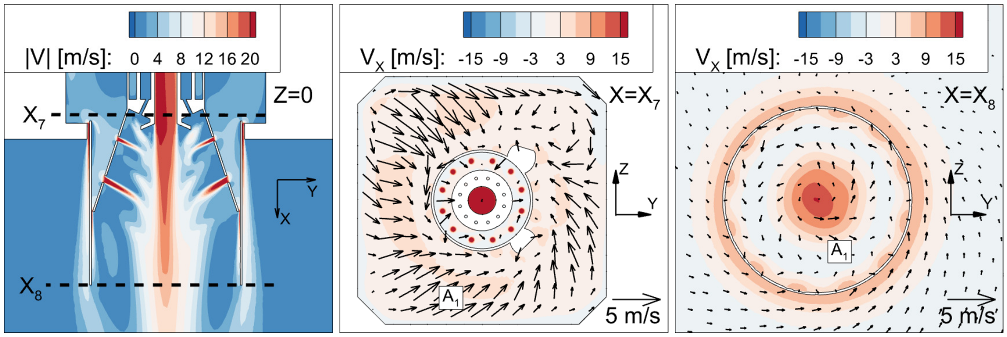

(a) Longitudinal section. (b) Axial section X7. (c) Axial section X8.

Fig. 17: Nozzle velocity field at V90 condition computed with RSM-BSL P-WR.

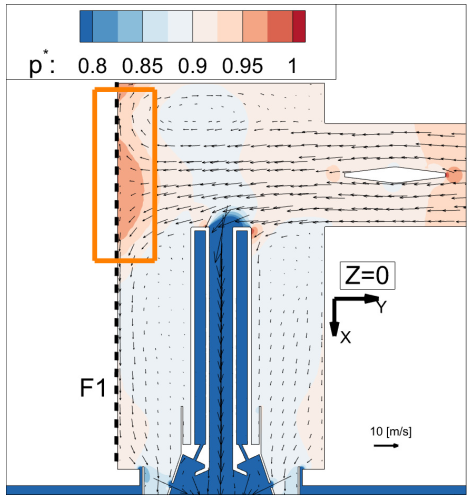

Fig. 18: Nondimensionalized static pressure field in burner case at V90 condition computed with RSM-BSL P-WR.

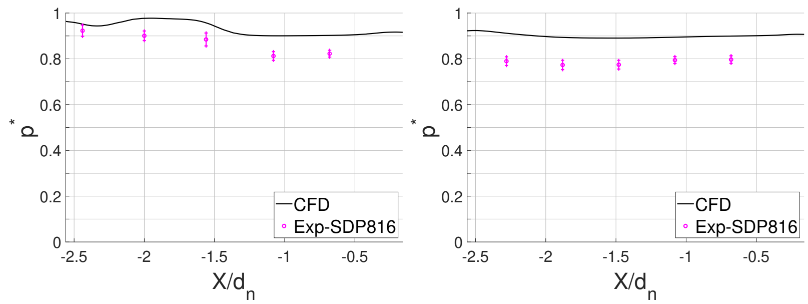

(a) Profiles on line F1.

(b) Profiles on line F4.

Fig. 19: Measured and RSM-BSL P-WR profiles of nondimensionalized static pressure at V90 condition.

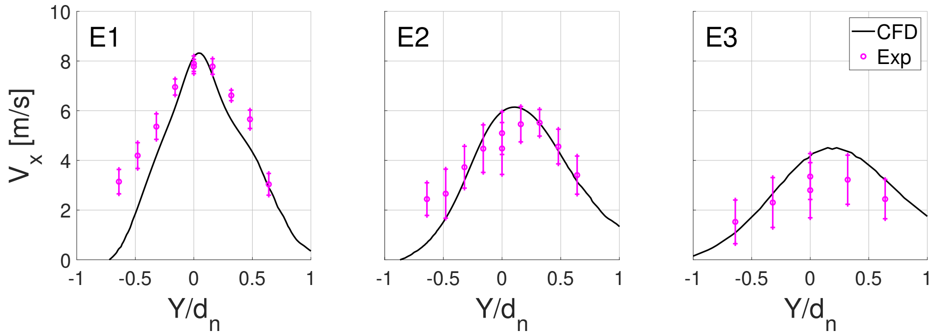

Fig. 20: Measured and RSM-BSL P-WR V_x profiles on transversal lines E1, E2, and E3 in combustion chamber at condition V90.

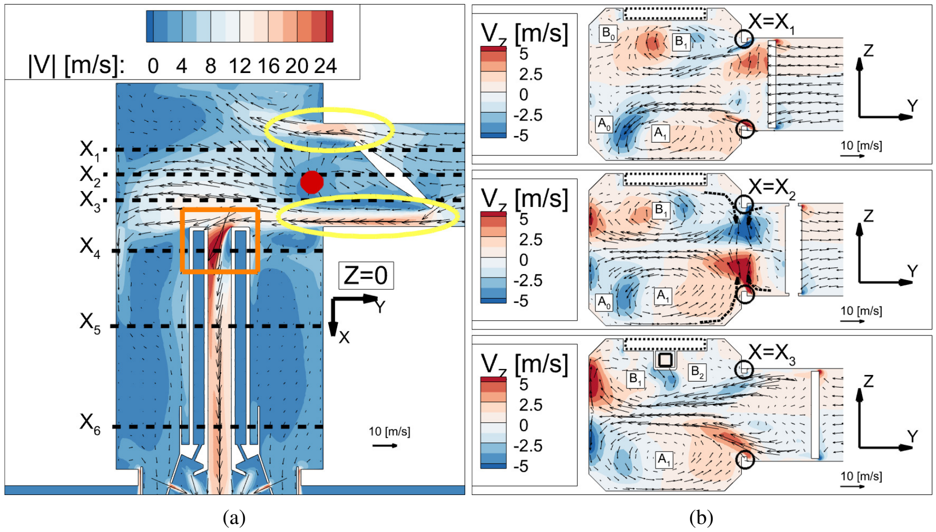

Fig. 21: Velocity field in burner case at V50 condition computed with RSM-BSL P-WR.

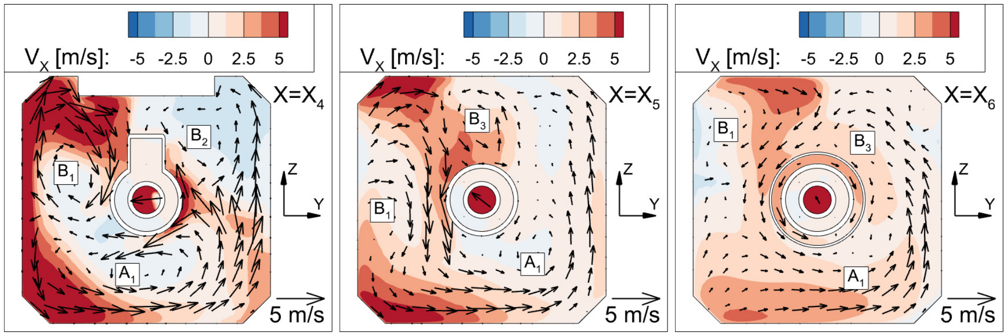

(a) Section X4. (b) Section X5. (c) Section X6.

Fig. 22: Velocity field in downstream part of burner case at V50 condition computed with RSM-BSL P-WR.

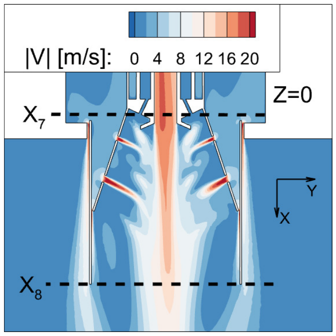

(a) Longitudinal section.

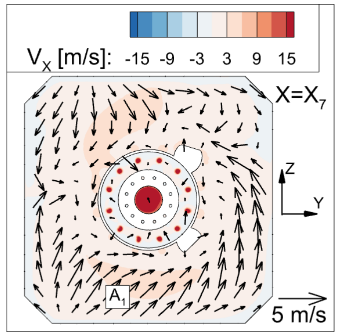

(b) Axial section X7.

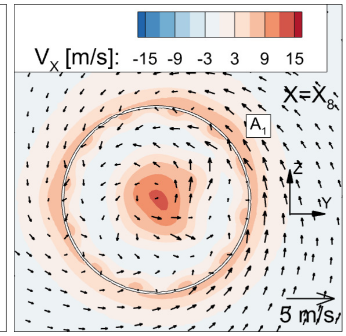

(c) Axial section X8.

Fig. 23: Nozzle velocity field at V50 condition computed with RSM-BSL P-WR.

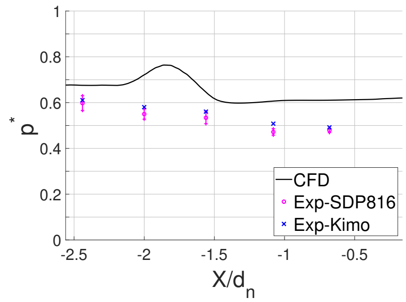

(a) Profiles on line F1.

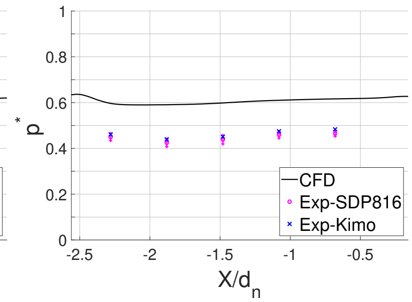

(b) Profiles on line F4.

Fig. 24: Measured and RSM-BSL P-WR profiles of nondimensionalized static pressure at V50 condition.

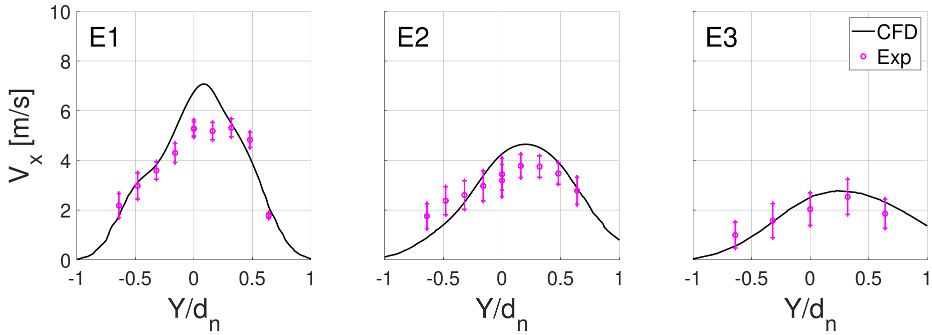

Fig. 25: Measured and RSM-BSL P-WR V_x profiles on transversal lines E1, E2 and E3 in combustion chamber at condition V50.